Lift Optimization Study of a Multi-Element Three-Segment Variable Camber Airfoil

Upender K. Kaul[*] and Nhan T. Nguyen[**]
NASA Ames Research Center, USA.

This paper reports a detailed computational high-lift study of the Variable Camber Continuous Trailing Edge Flap (VCCTEF) system carried out to explore the best VCCTEF designs, in conjunction with a leading edge flap called the Variable Camber Krueger (VCK), for take-off and landing. For this purpose, a three-segment variable camber airfoil employed as a performance adaptive aeroelastic wing shaping control effector for a NASA Generic Transport Model (GTM) in landing and take-off configurations is considered. The objective of the study is to define optimal high-lift VCCTEF settings and VCK settings/configurations. A total of 224 combinations of VCK settings/configurations and VCCTEF settings are considered for the inboard GTM wing, where the VCCTEFs are configured as a Fowler flap that forms a slot between the VCCTEF and the main wing. For the VCK settings of deflection angles of 55°, 60° and 65°, 18, 19 and 19 vck configurations, respectively, were considered for each of the 4 different VCCTEF deflection settings. Different vck configurations were defined by varying the horizontal and vertical distance of the vck from the main wing. A computational investigation using a Reynolds-Averaged Navier-Stokes (RANS) solver was carried out to complement a wind-tunnel experimental study covering three of of these configurations with the goal of identifying the most optimal high-lift configurations. Four most optimal high-lift configurations, corresponding to each of the VCK deflection settings, have been identified out of all the different configurations considered in this study yielding the highest lift performance.

Keywords: Variable Camber Continuous Trailing Edge Flap (VCCTEF), Drag Optimization, Generic Transport Model.

Nomenclature

α = angle of attack (AoA)
C_l = lift coefficient (total or sectional)
C_d = drag coefficient (total or sectional)
C_p = pressure coefficient: $2(p - p_\infty) / \rho V_\infty{}^2$
M = Mach number
Re = Reynolds number
M_∞ = free stream Mach number
V_∞ = free stream Velocity
VCK = Variable Camber Krueger, a high lift leading edge flap
VCCTEF = Variable Camber Continuous Trailing Edge
vck = refers to variable camber Krueger configurations
x = horizontal offset
y = vertical offset

* Computational Aerosciences Branch, NASA Advanced Supercomputing (NAS) Division; Associate Fellow, AIAA

** Intelligent Systems Division; Associate Fellow, AIAA

1 Introduction

The Advanced Air Transportation Technologies (AATT) project is conducting multidisciplinary foundational research to investigate advanced concepts and technologies for future aircraft systems under the Advanced Air Vehicle Program (AAVP) of the NASA Aeronautics Research Mission Directorate. A NASA study entitled "Elastically Shaped Future Air Vehicle Concept" was conducted in 2010[1,2] to examine new concepts that can enable active control of wing aeroelasticity to achieve drag reduction. This study showed that highly flexible wing aerodynamic surfaces can be elastically shaped in-flight by active control of wing twist and vertical deflection in order to optimize the local angle of attack of wing sections. Thus aerodynamic efficiency can be improved through drag reduction during cruise and enhanced lift performance during take-off and landing.

The study shows that active aeroelastic wing shaping control can have a potential drag reduction benefit. Conventional flap and slat devices inherently generate drag as they increase lift. The study shows that in cruise, conventional flap and slat systems are not aerodynamically efficient for use in active aeroelastic wing shaping control for drag reduction. A new flap concept, referred to as Variable Camber Continuous Trailing Edge Flap (VCCTEF) system, was conceived by NASA to address this need.[1] Initial study results indicate that the VCCTEF system may offer a potential pay-off in drag reduction in cruise that could provide significant fuel savings. Fig. 1 illustrates the VCCTEF deployed on the NASA generic transport model (GTM).

NASA and Boeing are currently conducting further studies of the VCCTEF under the research element Performance Adaptive Aeroelastic Wing (PAAW) within the AATT project.[3,4] This study built upon the development of the VCCTEF system (shown in Fig. 2) for the GTM[5] employs light-weight shaped memory alloy (SMA) technology for actuation and three separate chordwise flap segments shaped to provide a variable camber to the flap. Introduction of this camber has potential for drag reduction as compared to a conventional straight, plain flap. The flap is also made up of individual 2-foot spanwise sections, which enable different flap settings at each flap spanwise position. This enables wing twist shape control as a function of span to establish the best lift-to-drag ratio (L/D) at any aircraft gross weight or mission segment. Current wing twist on commercial transports is permanently set for one cruise, which is usually a 50% fuel loading or mid-point on the gross weight schedule. The VCCTEF offers different wing twist settings for each gross weight condition and also different settings for climb, cruise and descent, which is a major factor in obtaining the best L/D for all gross weight conditions and phases of flight. The second feature of VCCTEF is a continuous trailing edge. The individual 2-foot spanwise flap sections are connected with a flexible covering, so no breaks can occur in the flap platform, thus reducing excessive vorticity generation. This can reduce drag and airframe noise. Variable camber when combined with the continuous trailing edge results in a further reduction in drag.

The continuous trailing edge flap design combined with variable camber flap can result in lower drag. In summary, it can also offer a potential noise reduction benefit due to distinct optimal settings for climb, cruise and descent.

In a previous paper,[6] a computational study was conducted to explore the two-dimensional viscous effects in cruise of a number of VCCTEF configurations on lift and drag of the GTM wing section at the wing planform break. The flow solver OVERFLOW was used to conduct this study. The results identified the most aerodynamically efficient VCCTEF configuration among the initial candidates. The study also showed that a three-segment variable camber flap is aerodynamically more efficient than a single-element plain flap. A recent high-lift wind tunnel test conducted in July 2014 at University of Washington Aeronautical Laboratory[7,8] confirms this observation.

The present study explores the high-lift design space for the tri-element airfoil typical of a GTM wing section. The tri-element airfoil is comprised of VCK, main airfoil and the VCCTEF. The design space consists of 224 configurations drawn from various combinations of of VCK and VCCTEF settings, as described in the next section. Limited experimental data[7−10] are available corresponding to four configurations (VCK65, VCK60, VCK55, VCK50 – $vck1$), out of the 224 considered here computationally. In the following paragraphs, details of the computational methodology and computational grids used will be presented. In the high-lift flight configuration, we want to minimize the stall speed, which can be accomplished by maximizing C_l, and the results will be presented below in that context.

2 Methodology

The Reynolds-Averaged Navier-Stokes (RANS) solver, OVERFLOW, with the Spalart-Allmaras (SA) turbulence model[9] has been used for the current computational study. Grids were generated using the NASA Chimera Grid Tools (CGT).

Numerous combinations corresponding to 18 vck configurations for VCK setting (deflection angle) of 55° and 19 vck configurations each for VCK settings of 60° and 65° with respect to the main wing, and 4 VCCTEF settings with the Fowler slot for the inboard wing are considered in this study. These vck configurations along with the 4 VCCTEF settings are represented in Table 1 below. Three VCK settings are considered, corresponding to deflection angles of 55°, 60° and 65°. For each VCK setting, VCK55, VCK60 and VCK65, the vck configurations in terms of x and y displacement offset with respect to one experimental configuration (VCK65 + vck1) studied experimentally are shown in Fig. 3, Fig. 4 and Fig. 5, respectively. Nineteen vck configurations are designated vck1, vck2, vck3, ... , vck18, vck19. Detailed computational results discussing the lift characteristics will be shown below for all the 224 configurations to explore better design than the four studied experimentally.

Table 1: Definition of vck-VCCTEF Configurations

vck Configuration	10/10/10	15/10/5	20/5/5	30/0/0
vck1	vck1+10/10/10	vck1+15/10/5	vck1+20/5/5	vck1+30/0/0
vck2	vck2+10/10/10	vck2+15/10/5	vck2+20/5/5	vck2+30/0/0
vck3	vck3+10/10/10	vck3+15/10/5	vck3+20/5/5	vck3+30/0/0
vck4	vck4+10/10/10	vck4+15/10/5	vck4+20/5/5	vck4+30/0/0
vck5	vck5+10/10/10	vck5+15/10/5	vck5+20/5/5	vck5+30/0/0
——	————	————	————	————-
——	————	————	————	————-
——	————	————	————	————-
vck19	vck19+10/10/10	vck19+15/10/5	vck19+20/5/5	vck19+30/0/0
		vck configurations are represented in Fig. 4, Fig. 5 and Fig. 6		

Table 2: Definition of VCCTEF Configurations

Configuration	Notation	Flap 1, deg	Flap 2, deg	Flap 3, deg
3-segment circular arc camber	10/10/10	10	10	10
3-segment semi-rigid arc camber	15/10/5	15	10	5
3-segment	20/5/5	20	5	5
1-segment rigid flap	30/0/0	30	—	—
	Flap deflection angles are relative to the upstream segments			

Fig. 6 shows the four VCCTEF settings, corresponding to 4 different flap deflection angles, as shown in Table 2. Definition of various configurations are listed in Table 1. The four VCCTEF settings are denoted by 10/10/10, 15/10/5, 20/5/5 and 30/0/0.

3 Grid Sensitivity and Results

A grid sensitivity study using seven different grid levels was carried out with one configuration, VCK65/vck1 + VCCTEF-30/0/0, which corresponds to Fig. 5(a) and Fig. 6, where 30/0/0 is labeled 30 in Fig. 6. The grid resolution for the seven grids is shown in Table 3. First, the grid level 3 corresponding to the vck1+30/0/0 configuration is shown in Figs. 7(a,b,c) as a representative grid.

Fig. 8 shows the C_l vs α grid sensitivity results corresponding to the seven grids mentioned above. Results corresponding to grid levels 1, 2 and 3 shown in red, green and blue respectively, are appreciably different from the grid level 4, 5, 6 and 7 results, shown in magenta, cyan, black and black symbols, respectively.

Table 3: Grid Sensitivity: Grid Resolution of Six Different Grids

Grid Level	VCK	Main Wing	VCCTEF
1	210x87x3	311x87x3	233x87x3
2	258x96x3	475x96x3	271x96x3
3	263x106x3	652x106x3	295x106x3
4	436x106x3	694x106x3	471x106x3
5	639x106x3	694x106x3	471x106x3
6	639x106x3	694x106x3	625x106x3
7	639x114x3	837x114x3	625x114x3

But, results corresponding to grid levels 4, 5, 6 and 7 are practically the same. In the post-stall region any discrepancy among the various grid levels is ignored, since there are unsteady RANS effects that are not adequately resolved. So, in the rest of the paper, results shown will correspond to the grid level 4.

A total of 4x(19x2+18x1) = 224 cases (19 vck configurations for each of the two VCK settings, VCK65 and VCK60, 18 vck configurations for the VCK55 setting, all corresponding to 4 different VCCTEF settings) are considered. A sweep of angle of attack ranging from from -5 deg to 20 deg is considered. There are only 18 vck configurations in the case of VCK55, since the 19th configuration is unrealistic for this case. For all of the cases considered, grid level 4 was used for comparison of results, which are discussed below.

Instead of showing the results for all the 224 cases individually, a 2D bar graph is first presented showing C_{lmax} for the VCCTEF-10x10x10 setting in Fig. 9. Corresponding plot for C_{dmax} is shown in Fig. 10. Fig. 9 gives an overall view of the lift performance of the VCCTEF-10x10x10 setting for all the vck configurations corresponding to VCK55 and VCK60 and VCK65, and Fig. 10 shows corresponding results for C_{dmax}. Similarly, Fig. 11 and Fig. 12 show C_{lmax} and C_{dmax}, respectively, for the VCCTEF-15x10x5 setting. Fig. 13 and Fig. 14 show the corresponding results for the VCCTEF-20x5x5 setting, and Fig. 15 and Fig. 16 show the corresponding results for the VCCTEF-30x0x0 setting. Figs. 9 through 16 give an overall view of the C_{lmax} and C_{dmax} results for all the cases considered. The details of why these vck configurations yield distinctly different lift characteristics will be presented in a separate paper, where the corresponding flow fields will be studied in detail. The present paper is focussed on the design aspects of the problem.

Results for C_l vs α are shown for a subset of these 224 cases. For this purpose, cases giving 4 largest values of C_{lmax} are selected from Fig. 9 through Fig. 16. It turns out that for VCK55 setting, vck configurations of 2, 4, 14 and 15 give the largest C_{lmax} for all the four VCCTEF settings of 10x10x10, 15x10x5, 20x5x5 and 30x0x0, and for VCK60 and VCK65 settings, vck configurations of 2, 7, 15 and 19 give the largest C_{lmax} for all the four VCCTEF settings. Therefore, in the discussion of results below, only these vck configurations will be considered.

Before discussing the lift curves corresponding to these selected vck configurations, a test case corresponding to the VCCTEF setting of 30x0x0 and vck1 configuration was investigated for the α range of -5,-4,-3,-2,-1,0,5,10,11,12,13,....20. Fig. 17a and Fig. 17b show the C_l vs α and drag polar results, respectively. It is observed that a constant lift curve slope exists only beyond $\alpha = 0$, which shows that at lower angles of attack, the lift curve for the tri-element VCK-wing-VCCTEF system does not follow linear theory. This is shown by a nonlinear lift curve in the α range below 0 deg. In discussing the lift curve and drag polar results below, the α range of -5,0,5,10,11,12,13,....20 was considered.

Fig. 18(a,b) shows the C_l vs α and drag polar results, respectively, for the VCK55 and VCCTEF-10x10x10 settings corresponding to vck2, vck4, vck14 and vck15 configurations. The vck15 case consistently outperforms the other three, based on maximum C_l. As mentioned above, in high-lift flight configuration, we want to minimize the stall speed, which can be accomplished by maximizing C_l. The vck15 case also performs the best for the other three VCCTEF settings, 15x10x5, 20x5x5 and 30x0x0 for the VCK55 setting, as shown in Fig. 19(a,b), Fig. 20(a,b) and Fig. 21(a,b), respectively.

The situation is different for the VCK60 setting, where the best lift performance (C_{lmax} is demonstrated by the vck2 case for all the VCCTEF settings. This is shown in Fig. 22 through Fig. 25. For the VCK65 setting, best lift performance is demonstrated again by the vck15 case for all the VCCTEF settings, as shown in Fig. 26 through Fig. 29.

For the case of VCK55 setting, corresponding to the four best vck configurations, i.e., vck2, vck4, vck14

and $vck15$, various C_p plots are discussed below. Fig. 30(a), Fig. 30(b) and Fig. 30(c) show pressure distributions over the individual three elements of the tri-element airfoil, VCK, main wing and VCCTEF-20x5x5, respectively, each corresponding to the $vck2$, $vck4$, $vck14$ and $vck15$ configurations. Fig. 31(a), Fig. 31(b), Fig. 31(c) and Fig. 31(d) show consolidated pressure distributions over the tri-element system with the $vck2$, $vck4$, $vck14$ and $vck15$ configurations, respectively. The consolidated C_p plots show a direct comparison among the three elements of the tri-element airfoil on the same scale.

Fig. 31 shows the highest C_p corresponding to $vck2$ and next highest C_p for the $vck14$ configuration for the VCK flap; highest C_p corresponding to $vck4$ and next highest C_p for the $vck15$ configuration for the main wing; practically the same C_p for all the four vck configurations for the VCCTEF (20x5x5), with $vck15$ slightly outperforming the other three vck configurations. The overall result of this is shown in Fig. 20(a), where $vck15$ configuration yields the best high lift performance, followed by $vck2$ with the next best high lift performance. The inspection of C_p profiles is important since it is directly correlated to C_l.

Similarly, Fig. 32(a), Fig. 32(b) and Fig. 32(c) show pressure distributions over the three individual airfoil elements corresponding to the VCK60 setting and the VCCTEF-20x5x5 setting. Fig. 33(a), Fig. 33(b), Fig. 33(c) and Fig. 33(d) show consolidated pressure distributions over the tri-element corresponding to the four vck configurations, $vck2$, $vck7$, $vck15$ and $vck19$, as mentioned above. Fig. 32 shows the highest C_p corresponding to $vck2$ and next highest C_p for the $vck15$ configuration for the VCK flap; highest C_p corresponding to $vck15$ and next highest C_p for the $vck19$ configuration for the main wing; highest and the next highest C_p for $vck2$ and $vck15$, respectively, for the VCCTEF(20x5x5). The overall result of this is shown in Fig. 24(a), where $vck2$ and $vck15$ configurations yields the best and the next best high lift performance,

Fig. 34(a-c) and Fig. 35(a-d) show corresponding results for the VCK65 setting. Fig. 34 shows the highest C_p corresponding to $vck15$ and next highest C_p for the $vck2$ configuration for the VCK flap; highest C_p corresponding to $vck15$ and next highest C_p for the $vck2$ configuration for the main wing; highest and the next highest C_p for $vck15$ and $vck2$, respectively, for the VCCTEF (20x5x5). The overall result of this is shown in Fig. 28(a), where $vck15$ and $vck2$ configurations yields the best and the next best high lift performance. For the case of VCK65, all the three elements of the tri-element airfoil behave similarly, in terms of C_p distributions.

It is shown that $vck15$ and $vck2$ configurations are the top two candidates, in terms of overall high lift performance, out of all the three VCK settings (VCK55, VCK60 and VCK65) for the VCCTEF-20x5x5 setting. Fig. 29(a) further shows that the VCCTEF-30x0x0 setting gives the highest lift performance ($C_l - \alpha$) corresponding to $vck15$ and $vck2$ configurations out of all the 4 VCCTEF settings.

4   Summary

In the present study, we explored, using RANS calculations, various design configurations of the three-element GTM airfoil, consisting of 19 vck configurations corresponding to each of the two VCK settings (VCK60 and VCK65), and 18 vck configurations corresponding to the VCK55 setting and 4 VCCTEF settings with the Fowler slot on the inboard section of the wing. We have identified two topmost vck configurations corresponding to each of the three VCK settings. For all the VCK settings, $vck2$ and $vck15$ give the best lift performance, regardless of the four VCCTEF settings used. In particular, the VCCTEF-30x0x0 setting gives the highest overall lift performance with the $vck2$ and $vck15$ configurations. Thus, the best configurations for the GTM airfoil have been identified out of all the 224 cases studied. This provides a useful guide for the wind-tunnel experiment to verify the best design GTM configurations. Some of these best high-lift configurations offer a counter-intuitive design that would not have been considered experimentally *a priori*.

5   Acknowledgement

NNL12AD09T entitled "Development of Variable Camber Continuous Trailing Edge Flap System for B757 Configured with a More Flexible Wing."

6   References

[1]Nguyen, N., "Elastically Shaped Future Air Vehicle Concept," NASA Innovation Fund Award 2010 Report, October 2010, Submitted to NASA Innovative Partnerships Program. http://ntrs.nasa.gov/archive/nasa/casi.ntrs.nasa.g

[2]Nguyen, N., Trinh, K., Reynolds, K., Kless, J., Aftosmis, M., Urnes, J., and Ippolito, C., "Elastically Shaped Wing Optimization and Aircraft Concept for Improved Cruise Efficiency," AIAA Aerospace Sciences Meeting, AIAA-2013-0141, January 2013.

[3]Boeing Report No. 2012X0015, "Development of Variable Camber Continuous Trailing Edge Flap System," October 4, 2012.

[4]Urnes, J., Nguyen, N., Ippolito, C., Totah, J., Trinh, K., and Ting, E., "A Mission Adaptive Variable Camber Flap Control System to Optimize High Lift and Cruise Lift to Drag Ratios of Future N+3 Transport Aircraft," AIAA Aerospace Sciences Meeting, AIAA-2013-0214, January 2013.

[5]Jordan, T. L., Langford, W. M., Belcastro, C. M., Foster, J. M., Shah, G. H., Howland, G., and Kidd, R., "Development of a Dynamically Scaled Generic Transport Model Testbed for Flight Research Experiments," AUVSI Unmanned Unlimited, Arlington, VA, 2004.

[6]Kaul, U. K. and Nguyen, N. T., "Drag Optimization Study of Variable Camber Continuous Trailing Edge Flap (VCCTEF) Using OVERFLOW," AIAA 2014-2444, 32nd Applied Aerodynamics Conference, Atlanta, GA, June 2014

[7]Nguyen, N. T., Precup, N., Livne, L., Urnes, J., Dickey, E., Nelson, C., Chiew, J., Rodriguez, D., Ting, E., and Lebofsky, S., "Wind Tunnel Investigation of a Flexible Wing High-Lift Configuration with a Variable Camber Continuous Trailing Edge Flap Design," 33rd AIAA Applied Aerodynamics Confererence, AIAA-2015-2417, June 2015.

[8]Nguyen, N., Precup, N., Urnes, J., Nelson, C., Lebofsky, S., Ting, E., and Livne, E., "Experimental Investigation of a Flexible Wing with a Variable Camber Continuous Trailing Edge Flap Design," 32nd AIAA Applied Aerodynamics, AIAA 2014-2441, June 2014.

[9]Nguyen, N., Ting, E., and Lebofsky, S., "Aeroelastic Analysis of Wind Tunnel Test Data of a Flexible Wing with a Variable Camber Continuous Trailing Edge Flap," 56th AIAA/ASME/ASCE/AHS/ASC Structures, Structural Dynamics, and Materials Conference, AIAA-2015-1405, January 2015.

[10] Nathan Precup, Marat Mor and Eli Livne, "The Design, Construction, and Tests of a Concept Aeroelastic Wind Tunnel Model of a High-Lift Variable Camber Continuous Trailing Edge Flap (HL-VCCTEF) Wing Configuration," AIAA 2015-1406, 56th AIAA/ASCE/AHS/ASC Structures, Structural Dynamics, and Materials Conference 5-9 January 2015, Kissimmee, Florida,

[11]Spalart, P. R., and Allmaras, S. R., "A One-Equation Turbulence Model for Aerodynamic Flows," AIAA 92-0439, AIAA 30th Aerospace Sciences Meeting and Exhibit, Reno, NV , January 1992.

[12]Chiew, Jonathan, private communication, 2014

7 Figures
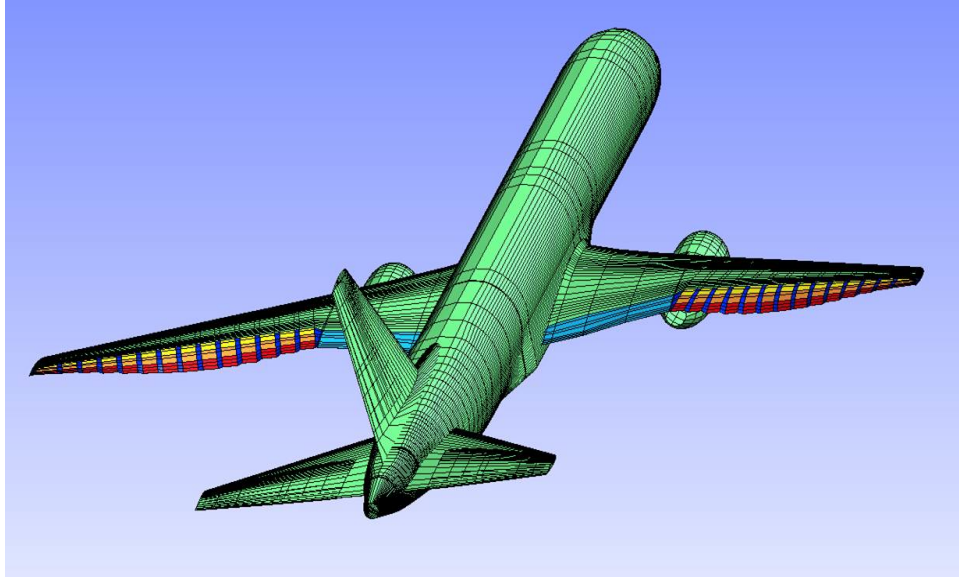
Figure 1: VCCTEF deployed on the generic transport model (GTM).
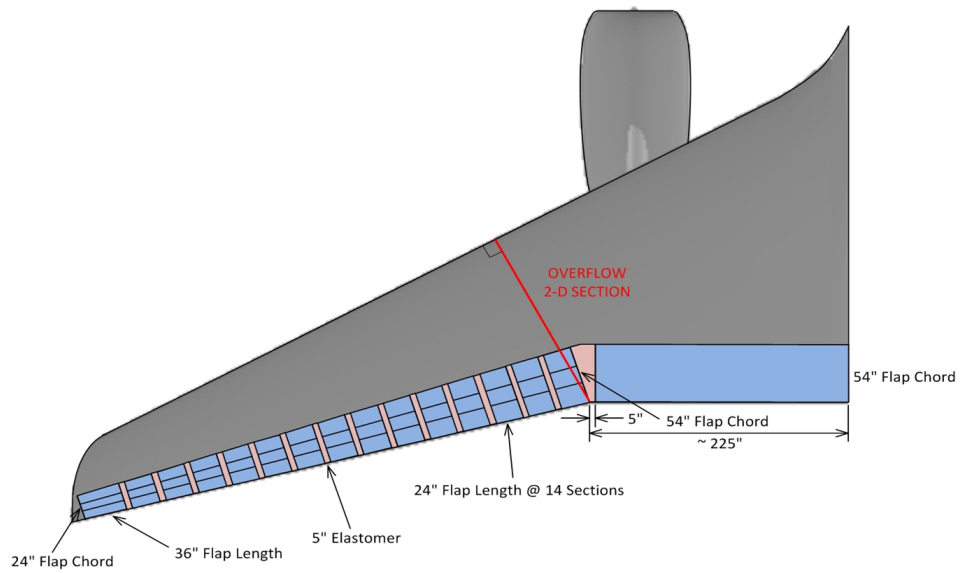
Figure 2: NASA/Boeing VCCTEF Configuration.
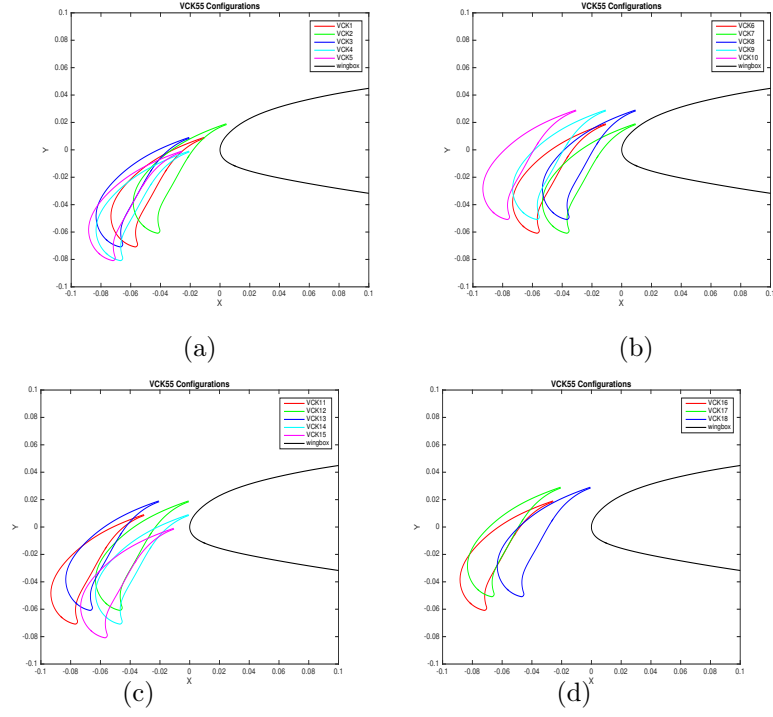
Figure 3: VCK55: Various *vck* configurations.
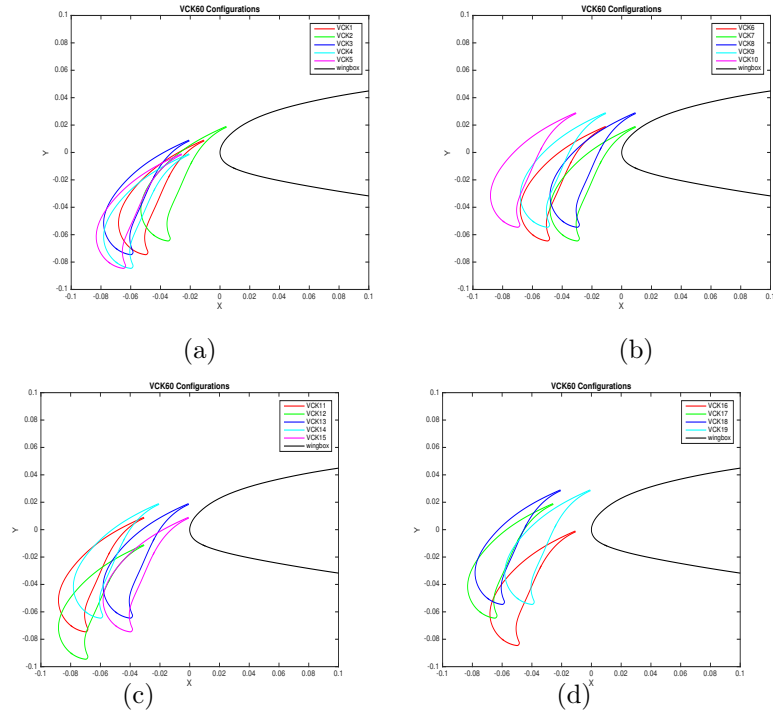
Figure 4: VCK60: Various *vck* configurations.
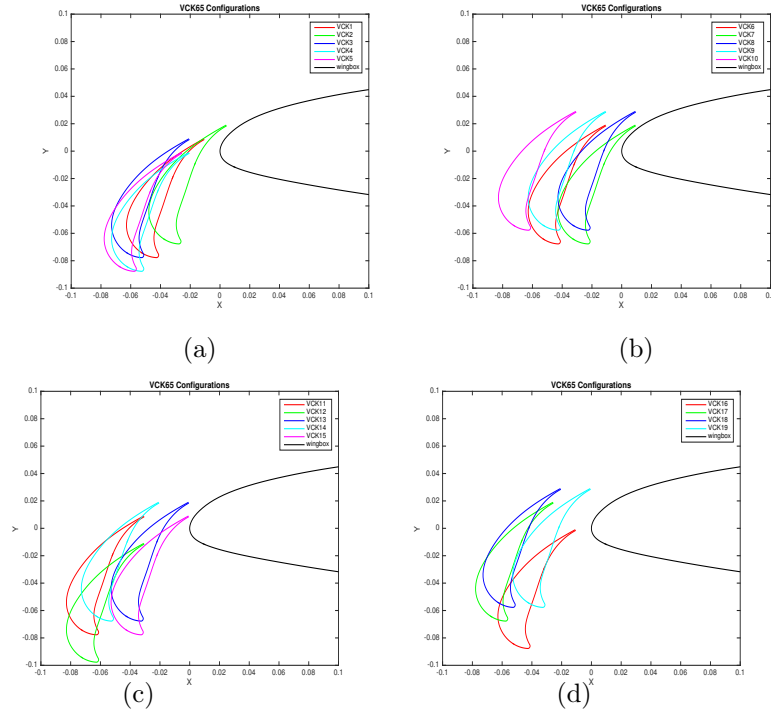
Figure 5: VCK65: Various *vck* configurations.
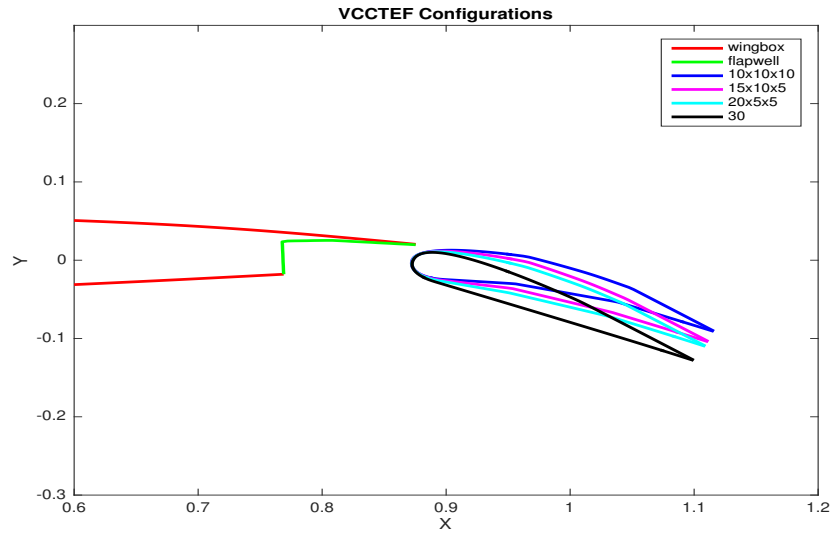
Figure 6: Four VCCTEF settings.
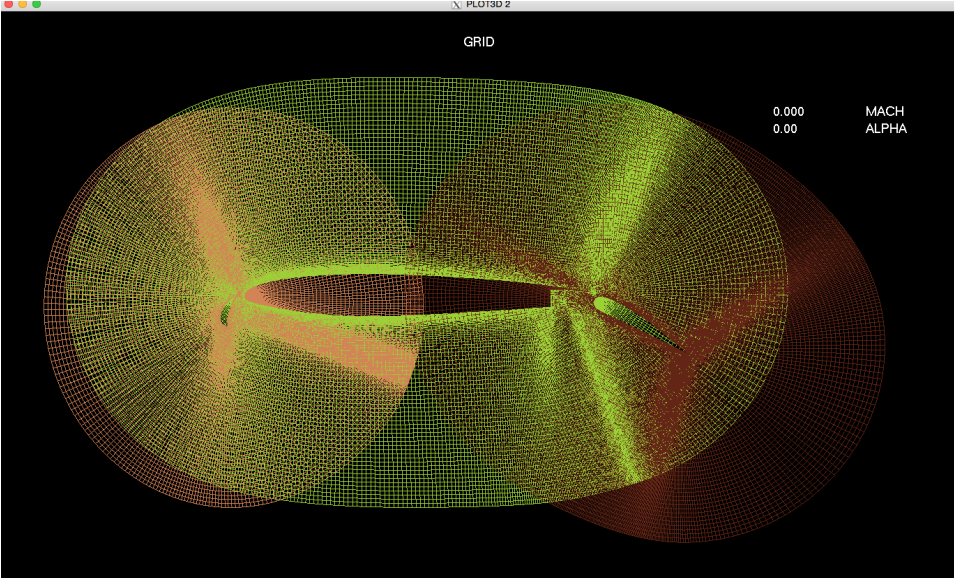
(a) Complete grid
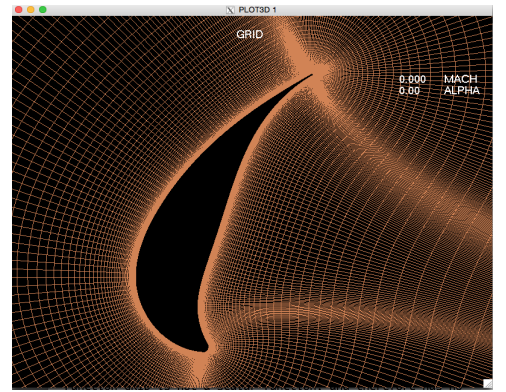
(b) VCK grid
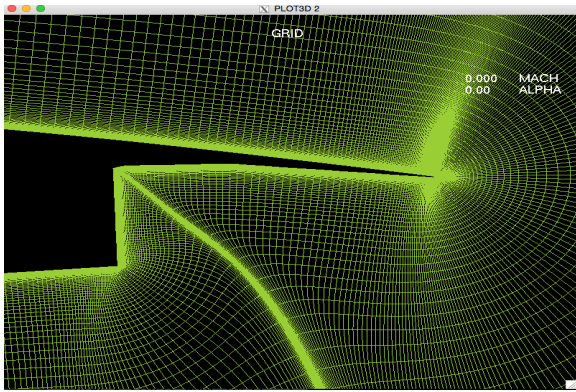
(c) Grid over flap well
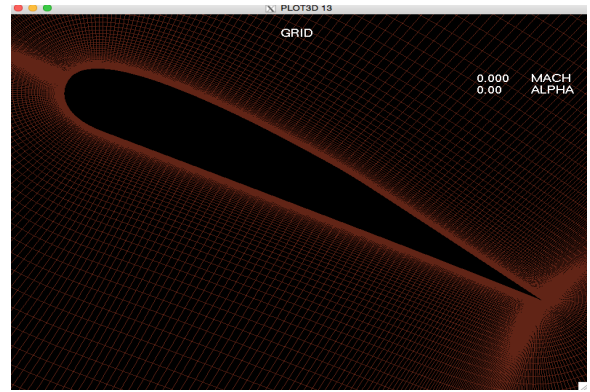
(d) Grid over VCCTEF

Figure 7: Perspective views of model geometry and representative grids
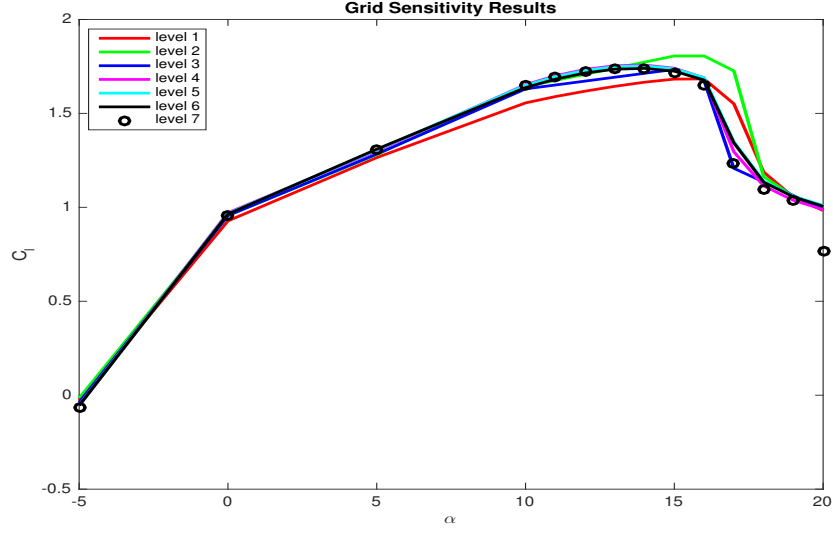
Figure 8: Comparison using seven grid levels: results in terms of C_l vs α
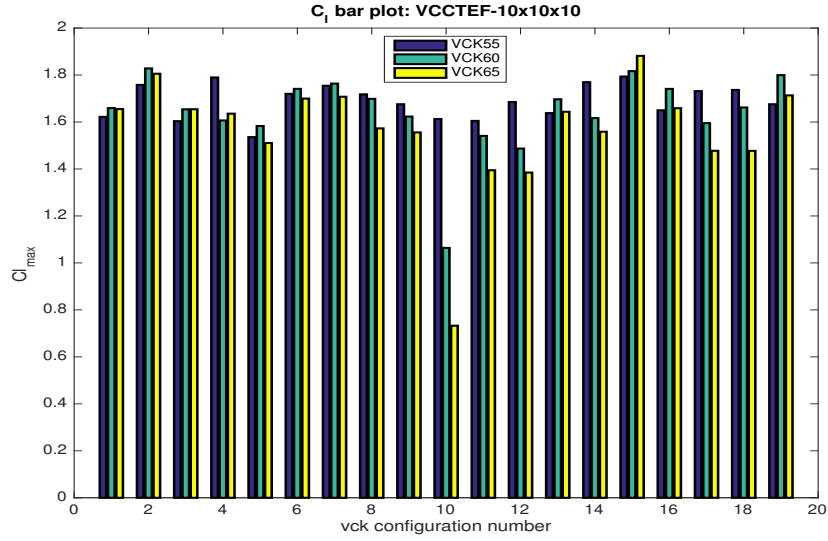
Figure 9: Bar graph showing C_{lmax} for VCCTEF-10x10x10 setting
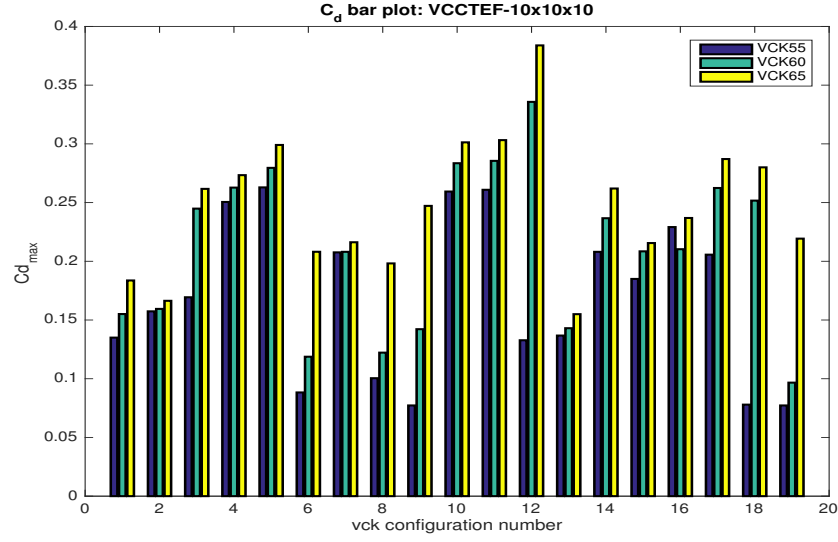
Figure 10: Bar graph showing C_{dmax} for VCCTEF-10x10x10 setting
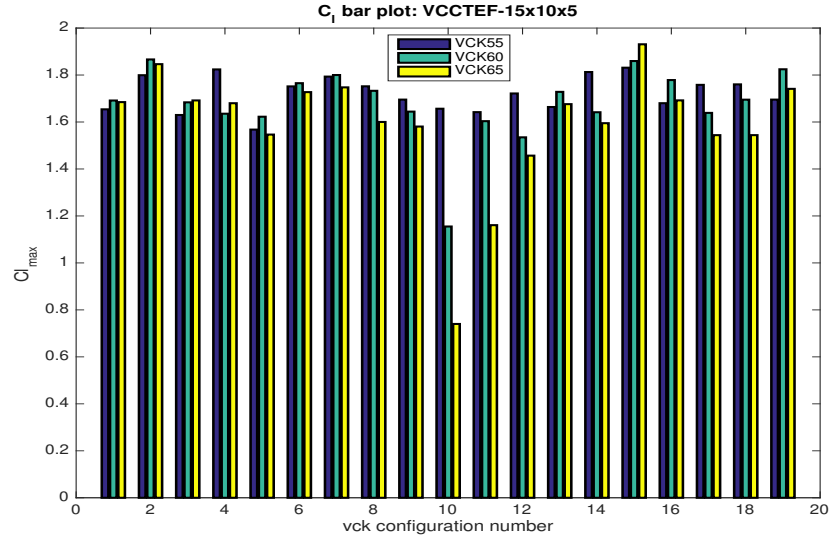
Figure 11: Bar graph showing C_{lmax} for VCCTEF-15x10x5 setting
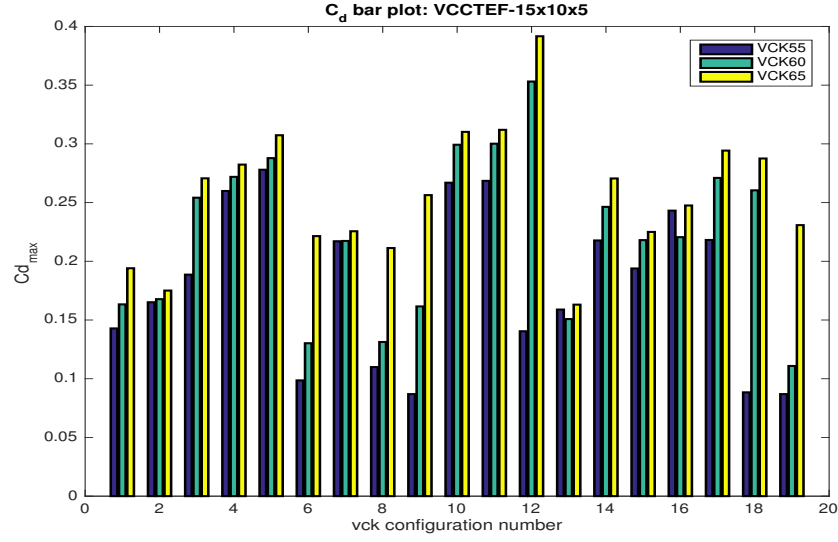
Figure 12: Bar graph showing C_{dmax} for VCCTEF-15x10x5 setting
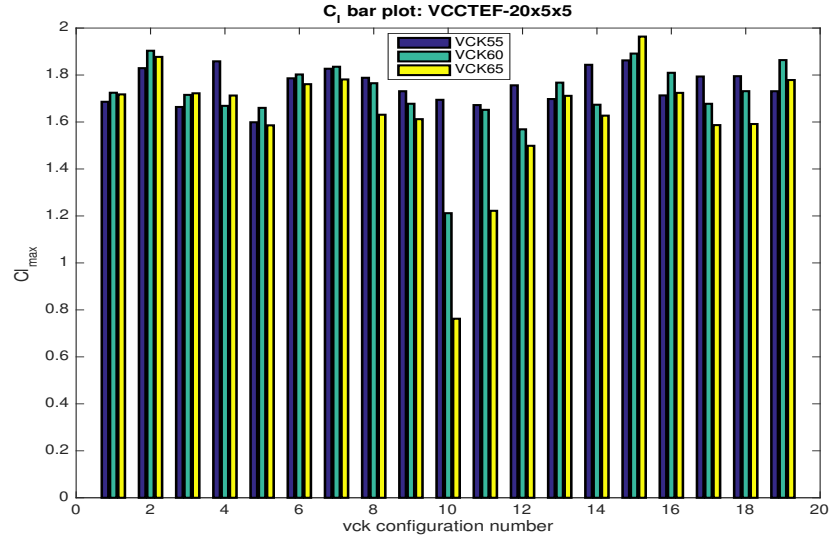
Figure 13: Bar graph showing C_{lmax} for VCCTEF-20x5x5 setting
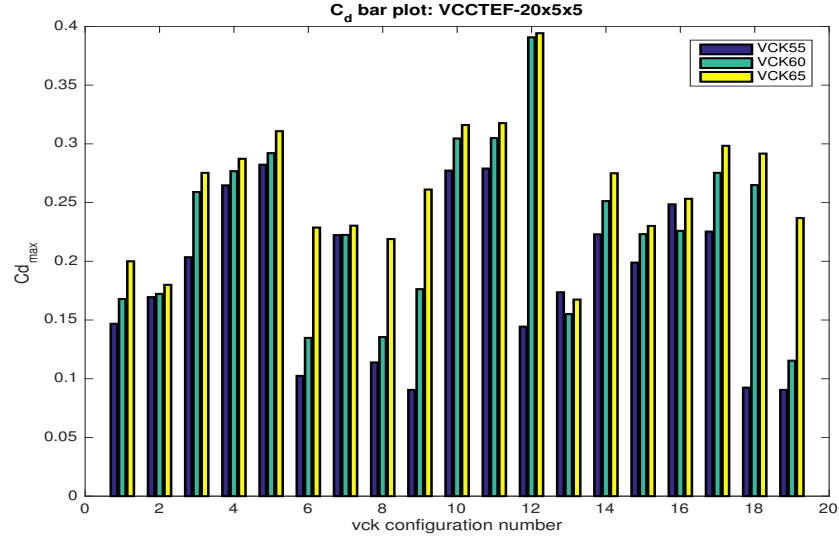
Figure 14: Bar graph showing C_{dmax} for VCCTEF-20x5x5 setting
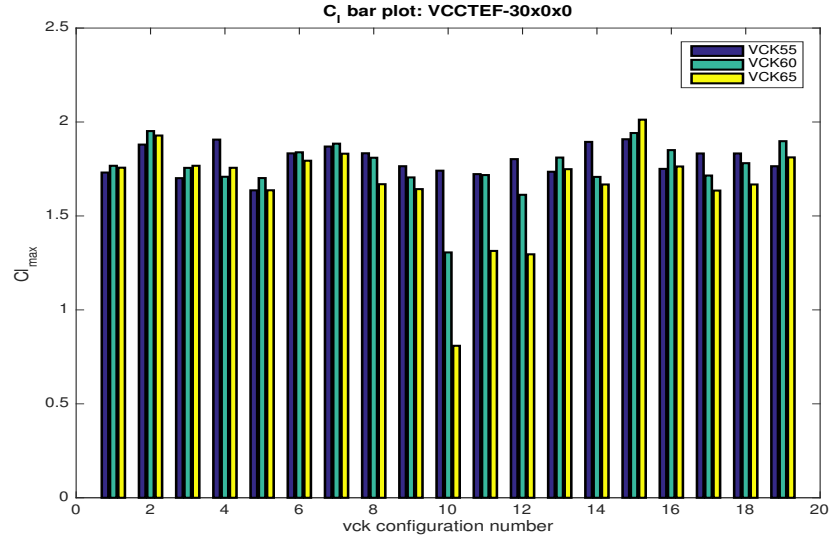
Figure 15: Bar graph showing C_{lmax} for VCCTEF-30x0x0 setting

14
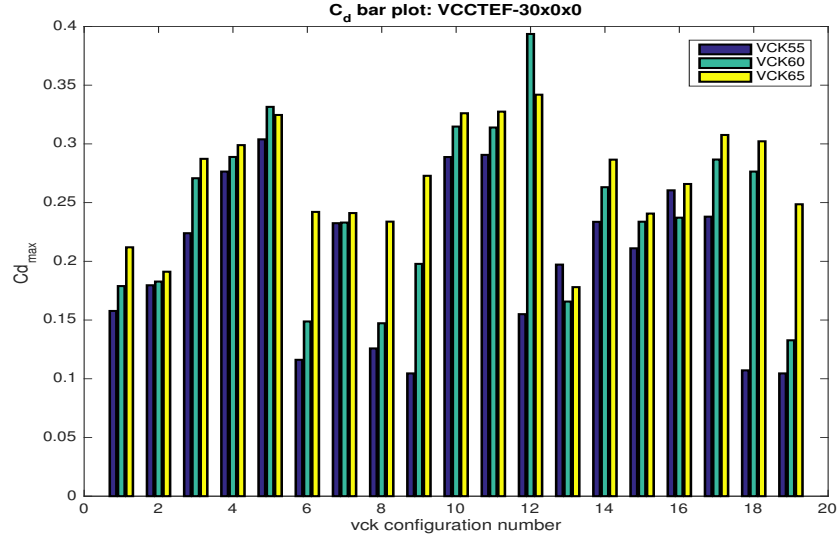
Figure 16: Bar graph showing C_{dmax} for VCCTEF-30x0x0 setting
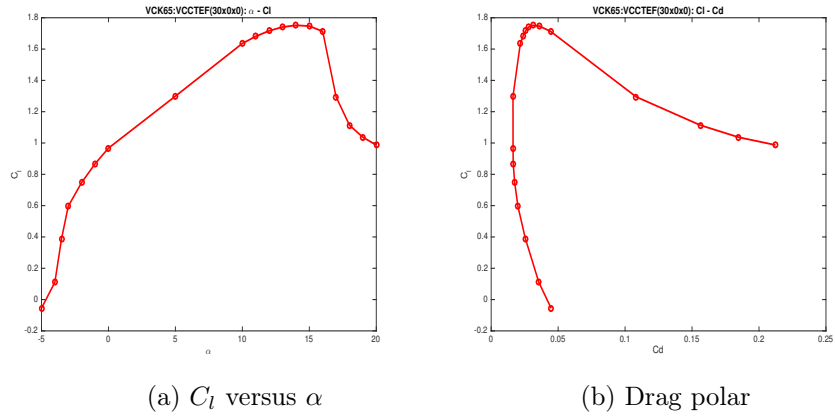
(a) C_l versus α

(b) Drag polar

Figure 17: VCK65 results for the vck1 configuration and VCCTEF-30x0x0 setting
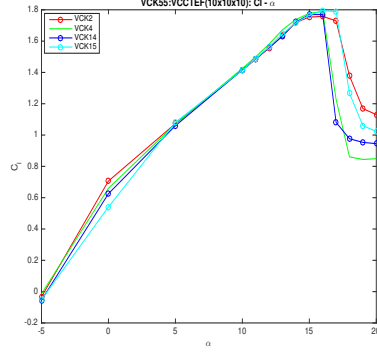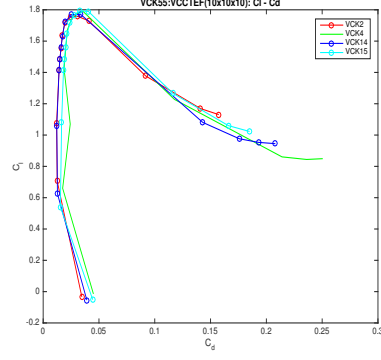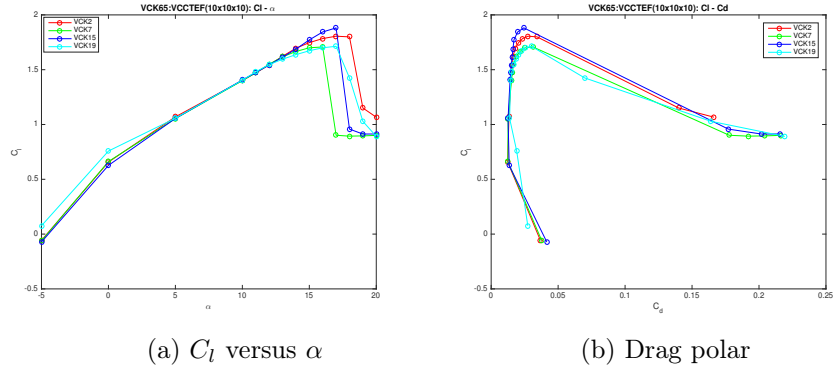
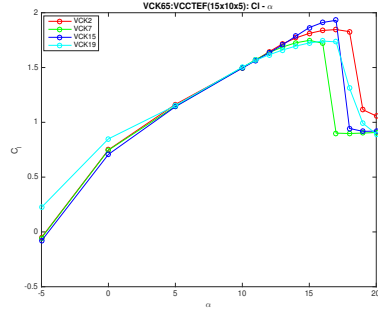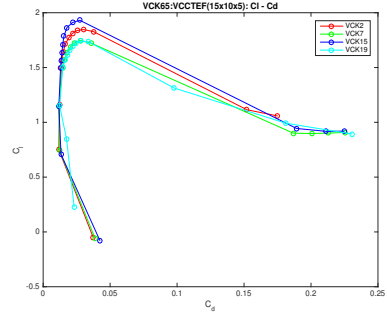(a) C_l versus α (b) Drag polar

Figure 18: VCK55 results for the VCCTEF-10x10x10 setting
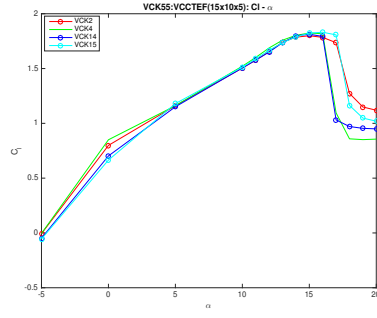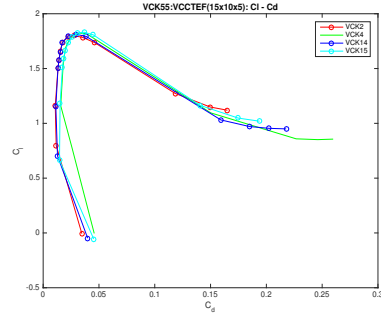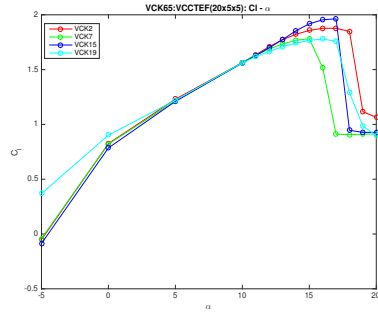

(a) C_l versus α (b) Drag polar

Figure 19: VCK55 results for the VCCTEF-15x10x5 setting
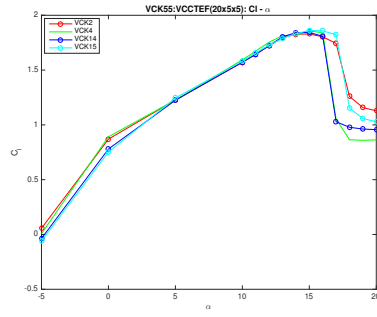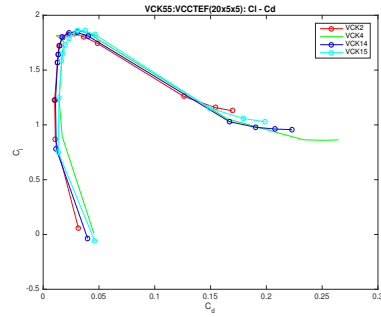
(a) C_l versus α (b) Drag polar

Figure 20: VCK55 results for the VCCTEF-20x5x5 setting
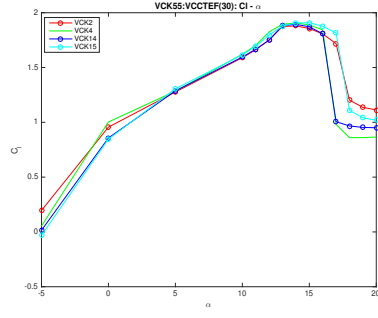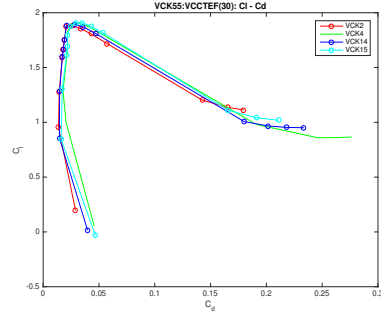
(a) C_l versus α (b) Drag polar

Figure 21: VCK55 results for the VCCTEF-30x0x0 setting
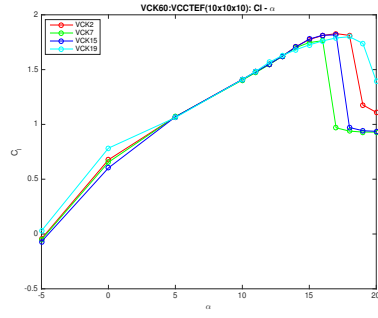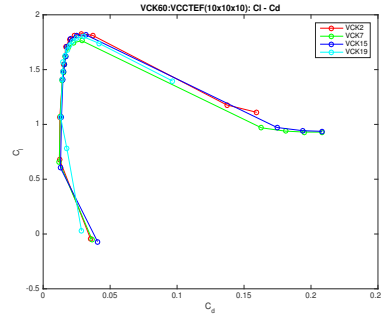
(a) C_l versus α (b) Drag polar

Figure 22: VCK60 results for the VCCTEF-10x10x10 setting
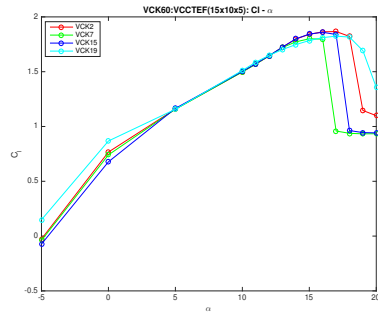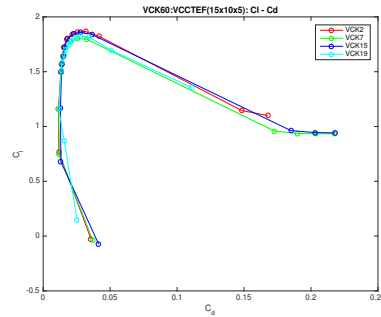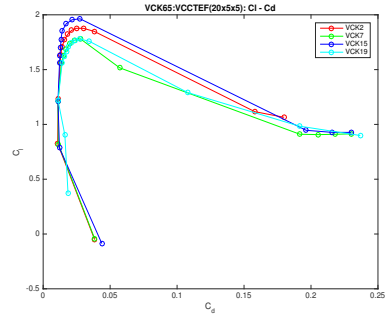

(a) C_l versus α (b) Drag polar

Figure 23: VCK60 results for the VCCTEF-15x10x5 setting

(a) C_l versus α (b) Drag polar
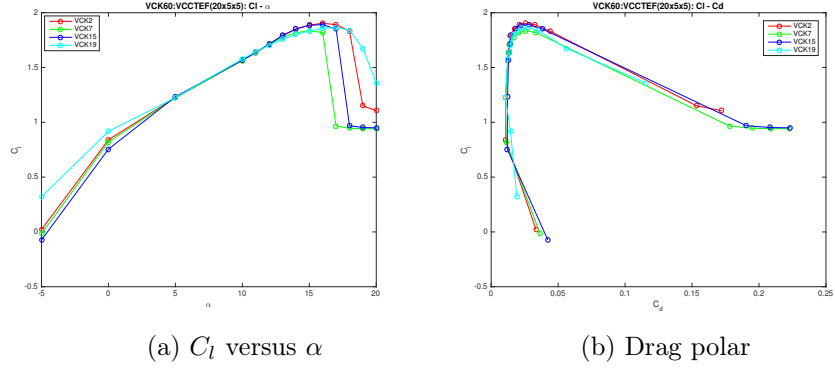
Figure 24: VCK60 results for the VCCTEF-20x5x5 setting

(a) C_l versus α (b) Drag polar
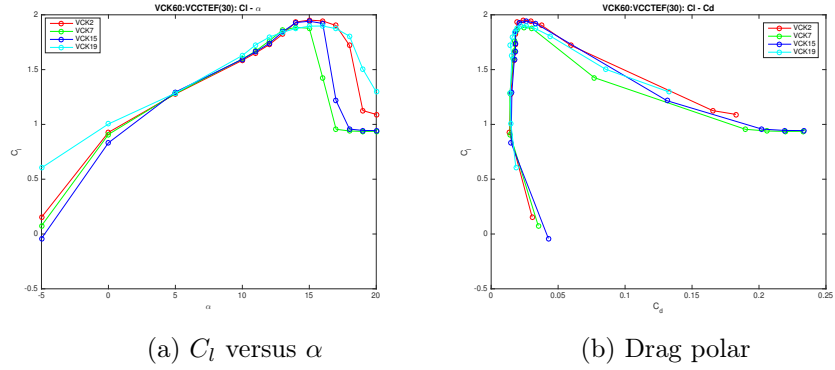
Figure 25: VCK60 results for the VCCTEF-30x0x0 setting

(a) C_l versus α (b) Drag polar

Figure 26: VCK65 results for the VCCTEF-10x10x10 setting

(a) C_l versus α (b) Drag polar

Figure 27: VCK65 results for the VCCTEF-15x10x5 setting

(a) C_l versus α (b) Drag polar

Figure 28: VCK65 results for the VCCTEF-20x5x5 setting
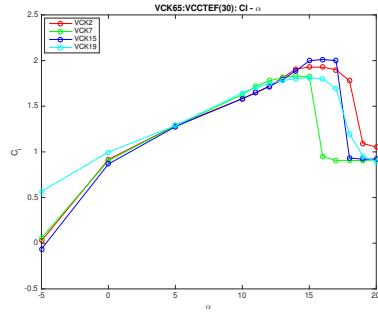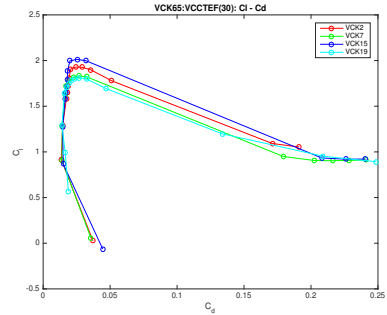
(a) C_l versus α (b) Drag polar

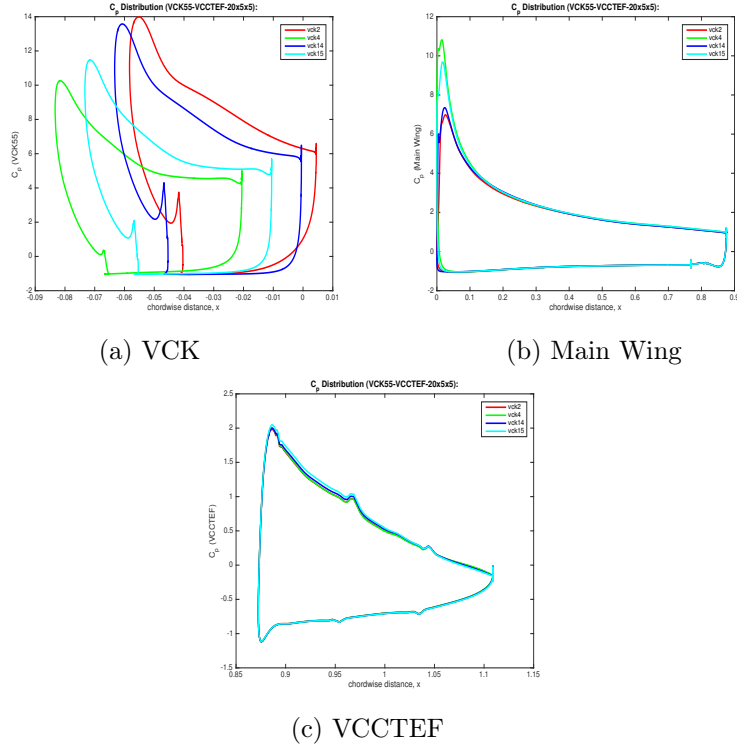Figure 29: VCK65 results for the VCCTEF-30x0x0 setting

(a) VCK

(b) Main Wing

(c) VCCTEF

Figure 30: VCK55 + VCCTEF-20x5x5: C_p distribution over individual airfoil element

(a) $vck2$

(b) $vck4$

(c) $vck14$

(d) $vck15$
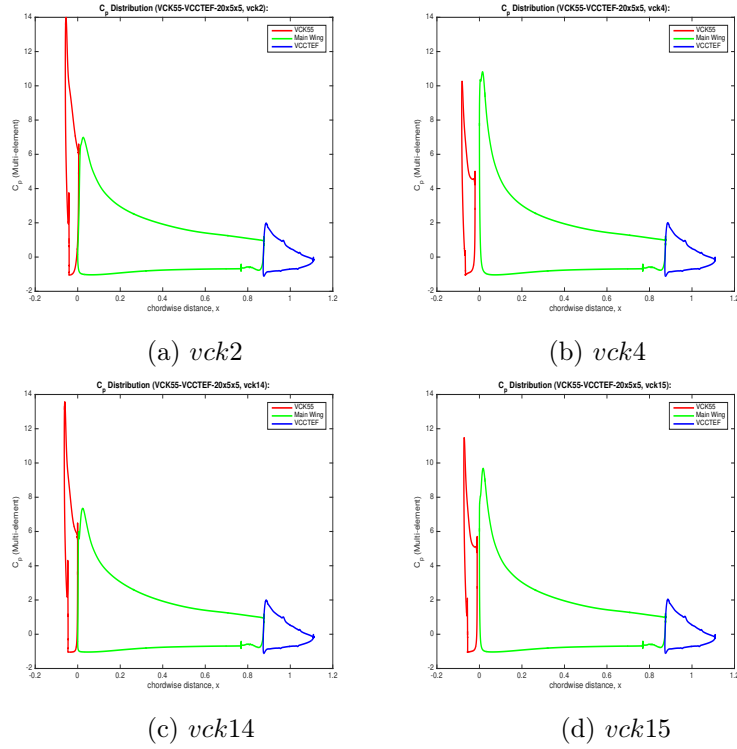
Figure 31: VCK55 + VCCTEF-20x5x5: consolidated C_p distribution over the multi-element airfoil

(a) VCK

(b) Main Wing
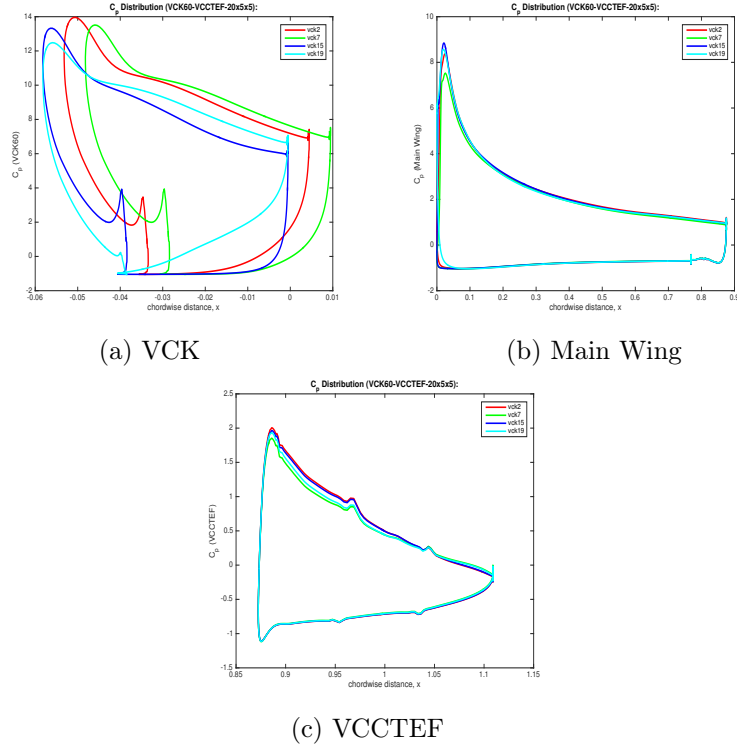
(c) VCCTEF

Figure 32: VCK60 + VCCTEF-20x5x5: C_p distribution over individual airfoil element

(a) $vck2$

(b) $vck7$

(c) $vck15$

(d) $vck19$
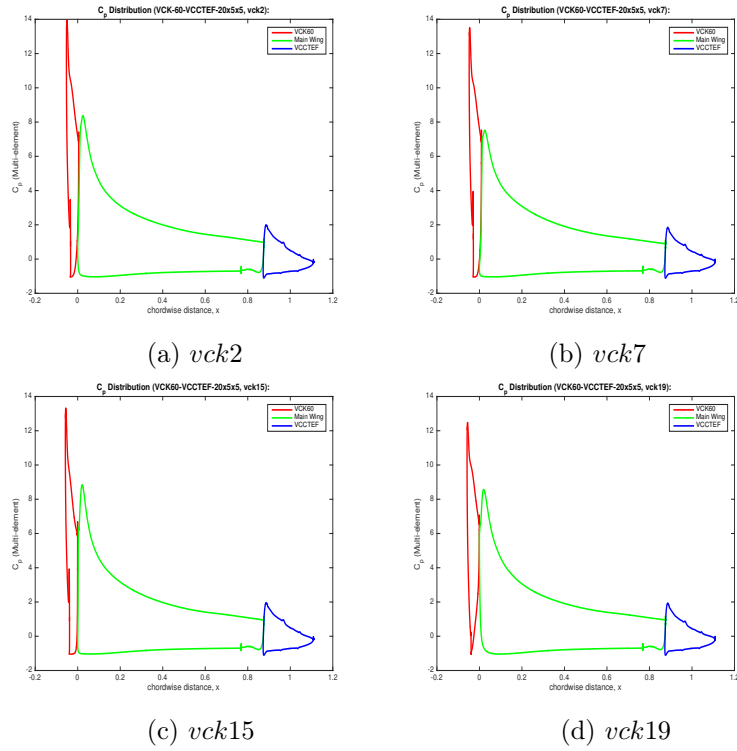
Figure 33: VCK60 + VCCTEF-20x5x5: consolidated C_p distribution over the multi-element airfoil

(a) VCK

(b) Main Wing
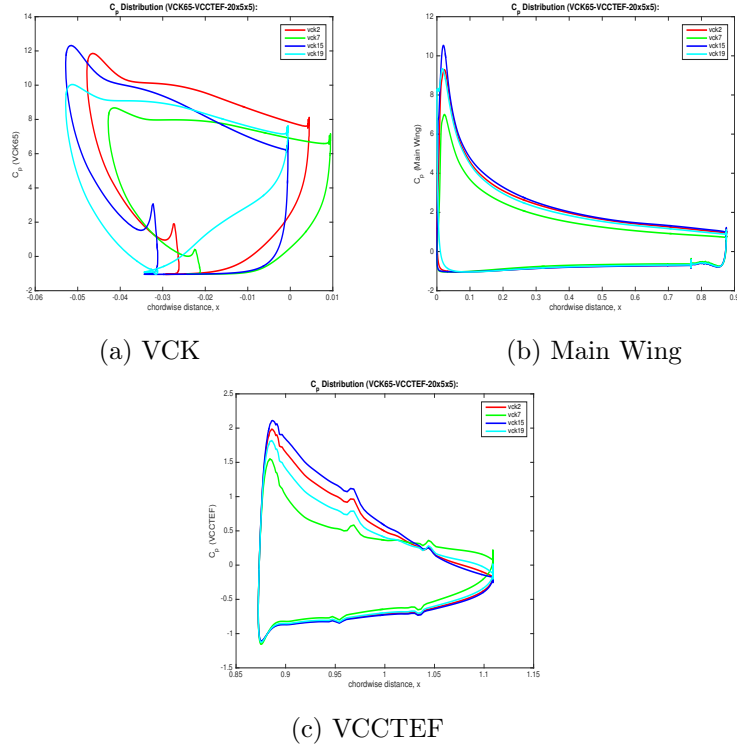
(c) VCCTEF

Figure 34: VCK65 + VCCTEF-20x5x5: C_p distribution over individual airfoil element

(a) $vck2$

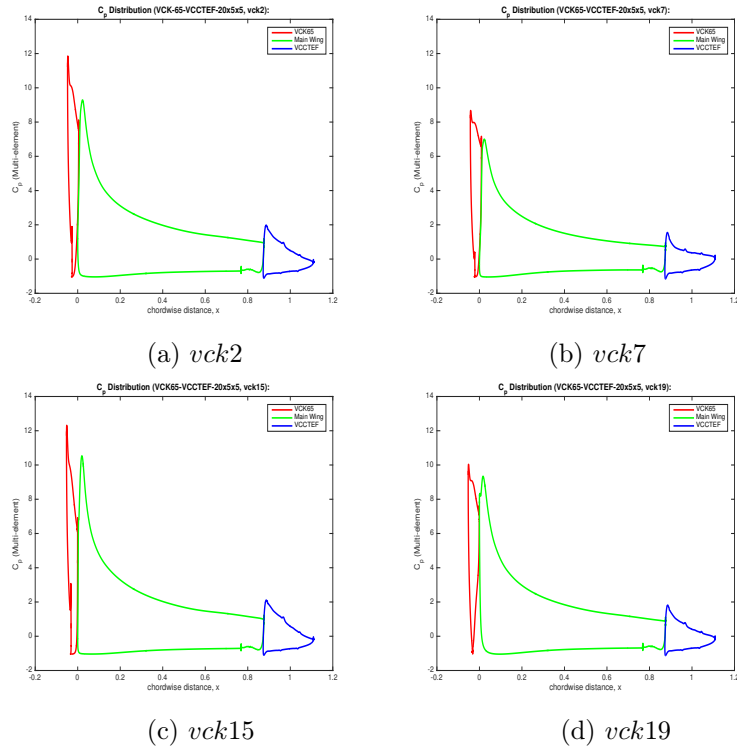
(b) $vck7$

(c) $vck15$

(d) $vck19$

Figure 35: VCK65 + VCCTEF-20x5x5: consolidated C_p distribution over the multi-element airfoil